

Identifying the source of spurious signals caused by B_0 inhomogeneities in single-voxel ^1H MRS

Zahra Shams¹ | Dennis W. J. Klomp¹ | Vincent O. Boer² |
Jannie P. Wijnen¹ | Evita C. Wiegers¹

¹Center for Image Sciences, University Medical Center Utrecht, Utrecht, The Netherlands

²Danish Research Centre for Magnetic Resonance, Centre for Functional and Diagnostic Imaging and Research, Copenhagen University Hospital Hvidovre, Hvidovre, Denmark

Correspondence

Zahra Shams, Center for Image Sciences, University Medical Center Utrecht, Heidelberglaan 100, 3508 GA, Utrecht, Netherlands.
Email: z.shams@umcutrecht.nl

Funding information

Eurostars Project E!12449 IMAGINE!

Purpose: Single-voxel MRS (SV MRS) requires robust volume localization as well as optimized crusher and phase-cycling schemes to reduce artifacts arising from signal outside the volume of interest. However, due to local magnetic field gradients (B_0 inhomogeneities), signal that was dephased by the crusher gradients during acquisition might rephase, leading to artifacts in the spectrum. Here, we analyzed this mechanism, aiming to identify the source of signals arising from unwanted coherence pathways (spurious signals) in SV MRS from a B_0 map.

Methods: We investigated all possible coherence pathways associated with imperfect localization in a semi-localized by adiabatic selective refocusing (semi-LASER) sequence for potential rephasing of signals arising from unwanted coherence pathways by a local magnetic field gradient. We searched for locations in the B_0 map where the signal dephasing due to external (crusher) and internal (B_0) field gradients canceled out. To confirm the mechanism, SV-MR spectra ($TE = 31$ ms) and 3D-CSI data with the same volume localization as the SV experiments were acquired from a phantom and 2 healthy volunteers.

Results: Our analysis revealed that potential sources of spurious signals were scattered over multiple locations throughout the brain. This was confirmed by 3D-CSI data. Moreover, we showed that the number of potential locations where spurious signals could originate from monotonically decreases with crusher strength.

Conclusion: We proposed a method to identify the source of spurious signals in SV ^1H MRS using a B_0 map. This can facilitate MRS sequence design to be less sensitive to experimental artifacts.

KEYWORDS

^1H MRS, B_0 inhomogeneity gradients, coherence pathways, spurious signals

1 | INTRODUCTION

^1H MRS is a powerful technique for noninvasive measurement of metabolite levels that can be applied in different

parts of the body such as brain, liver, and breast.¹ ^1H MRS can also provide diagnostic and prognostic information,

This is an open access article under the terms of the Creative Commons Attribution-NonCommercial-NoDerivs License, which permits use and distribution in any medium, provided the original work is properly cited, the use is non-commercial and no modifications or adaptations are made.

© 2022 The Authors. *Magnetic Resonance in Medicine* published by Wiley Periodicals LLC on behalf of International Society for Magnetic Resonance in Medicine.

such as by assessing metabolic alterations in tumor tissue. Understanding these alterations can have a major impact on treatment planning and patient outcome.² ^1H MRS can, however, be challenging, as metabolite detection is sometimes obscured due to contamination by lipid signal contamination or incompletely suppressed water signals, especially in the body.³ In the head, large signals from water and extracranial lipids need to be suppressed to detect the signals of interest from lower concentrated brain metabolites. Although water and lipid suppression in the head is expected to be technically less challenging than in other organs, artifacts caused by signals outside the voxel may obscure the baseline and contaminate metabolite signals. Due to the lack of prior knowledge related to these factors (in the basis functions), accurate metabolite quantification can be sensitive to fitting parameters.⁴ Artifacts, therefore, cause inaccurate metabolite quantification. A careful mitigation of artifacts will improve the widespread use of MRS.⁵ This requires robust localization of the signal of interest while disposing all unwanted signals arising from unwanted coherence pathways outside the volume of interest (VOI).

One of the most successful localization techniques to date is the semi-localized by adiabatic selective refocusing (semi-LASER) sequence,^{6,7} which uses a slice-selective excitation along one axis, and two pairs of slice-selective refocusing pulses along the remaining orthogonal axes.⁸ Phase cycling is the traditional strategy for suppressing unwanted signals by repeating the same experiment with different phases of the RF pulses and the receiver.^{9,10} The signals from the desired coherence pathway will be added together, while signals arising from unwanted coherence pathways will be canceled out through subtraction. Considering the approximate seven orders of magnitude signal crushing that are needed in single-voxel (SV) MRS, care must be taken in the proper design of phase-cycling steps and crusher gradients used in the sequence. For sequences with a high number of RF pulses, at least 16 phase cycling steps are needed to remove unwanted signals. However, relying on subtraction of strong unwanted signals requires highly stable (motion-free) acquisitions. Next to phase cycling, magnetic field gradients are used as an effective method for the selection of signals arising from the desired coherence pathway and crushing of signals arising from unwanted coherence pathways. The design of these crusher gradient schemes is usually performed empirically in vivo in a few subjects before implementing the protocol for a clinical study and not on each subject individually.

In the brain, insufficient suppression of spurious signals (ie, signals arising from unwanted coherence pathways) leads to artifacts in SV-MRS data. These artifacts are most likely caused by the water signal coming from areas

outside the VOI.¹¹ The sources of these spurious signals in MRS have been studied for the point resolved spectroscopy (PRESS) sequence via two different approaches. Moonen et al analyzed the source of spurious signals in PRESS using the coherence pathway formalism.¹² Later, the same theoretical description was used to design a set of experiments for the PRESS sequence that identified the coherence pathways associated with artifacts.¹¹ In these experiments, all eight combinations of RF pulses at zero flip angle (to account for imperfect slice profile) or at a nominal flip angle (ie, the ideal situation) were investigated. In both studies, infinite sharp edges for the slice profiles were assumed. The second approach involved k-space analysis of spurious echoes. Starck et al described the origin of spurious echo artifacts by Fourier transform concept, considering a realistic slice profile of the RF pulses.¹³ Local gradients, caused by magnetic-field inhomogeneities, can reverse the phase dispersion by a crusher gradient, leading to a rephasing of the spurious signal during the acquisition.^{1,11,13} For the theoretical analysis of the effect of crusher and local magnetic field gradients on spurious signals, Starck et al used a PRESS sequence with a linear static gradient as a model for local magnetic field gradient. However, this method exploited at 1.5 T is not transferable to the ultrahigh magnetic fields (ie, 7 T) with nonlinear shim gradients, which lead to steeper gradients outside the VOI.

In this work, we propose a new strategy to identify the source of spurious signals in single-voxel ^1H MRS data, taking into account the intrinsic B_0 field inhomogeneities using a B_0 field map at subcentimeter resolution. To predict the potential refocusing of spurious signals, we searched for areas where the signal dephasing caused by the local magnetic field gradients canceled the signal dephasing due to the crusher gradients. We compared the distribution of the source of spurious signals using two B_0 shimming conditions: VOI and whole-brain shimming (second order). Based on the resulting data, the number of regions from which a spurious signal could arise at different strengths of the crusher gradients was quantified. Our results provide a framework that can enable subject-specific and location-specific design of an optimal crusher gradient scheme in SV MRS.

2 | THEORY

To explain the effects of unwanted coherence pathways, we will consider the example of the semi-LASER sequence. Assuming that the excitation pulse, and all four refocusing pulses, of the semi-LASER sequence are calibrated with respect to the applied B_1^+ field, the VOI (area 1 in

Figure 1B) experiences a 90° excitation and complete refocusing by two pairs of refocusing pulses (90°, 180°, 180°, 180°, and 180°). However, the flip angle of a given pulse typically deviates from the nominal flip angle. Furthermore, the slice profile of a selective RF pulse is generally imperfect and will never achieve infinite sharp edges. That means the transition band of a RF pulse experiences a continuum of flip angles from 0 to the nominal value. Both can result in spurious signals (ie, signals arising from unwanted coherence pathways). The selection of the desired signal, corresponding to the center of the three intersecting orthogonal planes (VOI), is achieved by implementing a set of crusher pairs surrounding each of the refocusing pulses. The total gradient area of the coherence pathway $[-1 \ 1 \ -1]$ associated with the desired signal equals zero in the VOI. The total gradient areas of all the other coherence pathways will not equal zero. If the signals through these pathways are rephased by the intrinsic magnetic-field inhomogeneity gradients at any time within the acquisition window, artifacts may appear in the spectrum.

Although the transition bands of the refocusing pulses may experience a range of flip angles (from 0° to 180°), to simplify our example, we will assume that all transition regions experience a 90° excitation. In doing this, 25 spatial areas that experience a different combination of RF pulses can be identified (Figure 1B). As the semi-LASER sequence consists of five RF pulses, a total number of 81 coherence pathways can be identified. The desired pathway is the one in which the net gradient area equals zero. All 81 pathways originate from at least one of the 25 areas in Figure 1B. For example, the pathway $[-1 \ -1 \ -1 \ -1 \ -1]$ originates from the areas 2, 6, 21 and 25, and the pathway $[-1 \ -1 \ -1 \ 1 \ -1]$ originates from of the spatial regions 7, 11, 16, 20 and 8, 10, 17, 19.

To investigate how a local magnetic field gradient could result in a spurious signal in the acquisition window, the total integral of the magnetic field inhomogeneity gradient over time (B_0 gradient-time integral) along the anterior–posterior (AP), right–left (RL), and feet–head (FH) directions can be calculated using a 3D B_0 field map from the human head. The phase accrual from the crusher gradient-time integral (crusher areas) as well as B_0 (intrinsic) gradient-time integral along each spatial axis depend on the specific coherence pathway, as RF pulses can generate changes of coherence order, e.g. (+/-). The total crusher area over three spatial axes for a pulse sequence of N RF pulses $\mathbf{G}_{\text{area,tot}} = [\mathbf{g}_{\text{area},1}; \dots; \mathbf{g}_{\text{area},n}]$ can be computed as follows:

$$\mathbf{g}_{\text{area},i} = \int_0^{\tau_i} \mathbf{g}_{\text{crusher},i}(t)dt, i \in \{1, \dots, n\}, \quad (1)$$

where $\mathbf{g}_{\text{crusher},i}$ is a vector representing each crusher gradient strength in mT m^{-1} , and τ_i is its corresponding duration in milliseconds. The effect of these crusher gradients through all k coherence pathways, described as accumulated phase ($\Phi_{\text{crusher}} = [\phi_{\text{crusher},1}; \dots; \phi_{\text{crusher},k}] \in \mathbb{R}^{k \times 3}$) in $\text{Hz cm}^{-1} \text{ ms}$, can be expressed as

$$\Phi_{\text{crusher}} = \gamma \mathbf{C} \mathbf{G}_{\text{area,tot}}, \quad (2)$$

where γ is the gyromagnetic ratio, and \mathbf{C} represents the concatenated matrix of all k coherence pathways, which is of size $k \times n$. The desired pathway (eg, j th row of Φ_{crusher}) is, for a well-designed crusher/phase-cycling combination, the only pathway that will not experience any phase accumulation by the crushers (ie, $\phi_{\text{crusher},j} = [0 \ 0 \ 0]$).

The phase accumulated by the B_0 inhomogeneity gradients over time through all pathways, $\Phi_{\text{inhom.gr}} = [\phi_{\text{inhom.gr},1}; \dots; \phi_{\text{inhom.gr},k}] \in \mathbb{R}^{k \times 3}$, can be expressed in the unit of $\text{Hz cm}^{-1} \text{ ms}$ as follows:

$$\Phi_{\text{inhom.gr}}(x, y, z; T) = \gamma \mathbf{C} \mathbf{t} \nabla B_0(x, y, z), \quad (3)$$

where (x, y, z) is the 3D spatial location; $\mathbf{t} = [t_{\text{RF2}} - t_{\text{RF1}}; \dots; t_{\text{RFn}} - t_{\text{RFn-1}}; T - t_{\text{RFn}}]$ is the time vector with elements corresponding to the RF pulse time intervals; T is a certain time in the acquisition window; and $\nabla B_0(x, y, z) = \left[\frac{\partial B_0(x,y,z)}{\partial x}, \frac{\partial B_0(x,y,z)}{\partial y}, \frac{\partial B_0(x,y,z)}{\partial z} \right]$ is the B_0 spatial gradient vector. Therefore, $\Phi_{\text{inhom.gr}}(x, y, z; T)$ is a matrix size of $k \times 3$ for one given voxel in the magnetic field map, and the accumulated phase can be computed for all voxels (3D), which will result in a 4D matrix.

The gradient-time integral caused by the magnetic field inhomogeneity over the three dimensions in any of the pathways i , $\phi_{\text{inhom.gr},i}(x, y, z; T)$, can extend for tens of milliseconds into the acquisition, giving a time window t_{reph} to potentially rephase signals from the originally dephased (crushed) pathway. If the magnitude of $\phi_{\text{crusher},i}$ satisfies

$$\begin{aligned} \|\phi_{\text{inhom.gr},i}(x, y, z; \text{TE})\| &\leq \|\phi_{\text{crusher},i}\| \\ &\leq \|\phi_{\text{inhom.gr},i}(x, y, z; \text{TE} + t_{\text{reph}})\|, \end{aligned} \quad (4)$$

then the magnetic field inhomogeneity gradient will cause a spurious signal if the signs of $\phi_{\text{crusher},i}$ and $\phi_{\text{inhom.gr},i}(x, y, z; \text{TE})$ are opposite along each orthogonal axes: $\text{sign}((\phi_{\text{inhom.gr},i}(x, y, z; \text{TE}))_x) \neq \text{sign}((\phi_{\text{crusher},i})_x)$ for the x axis and similarly for y and z axes. The same should also hold for the sign of the elements of the vectors $\phi_{\text{crusher},i}$ and $\phi_{\text{inhom.gr},i}(x, y, z; \text{TE} + t_{\text{reph}})$.

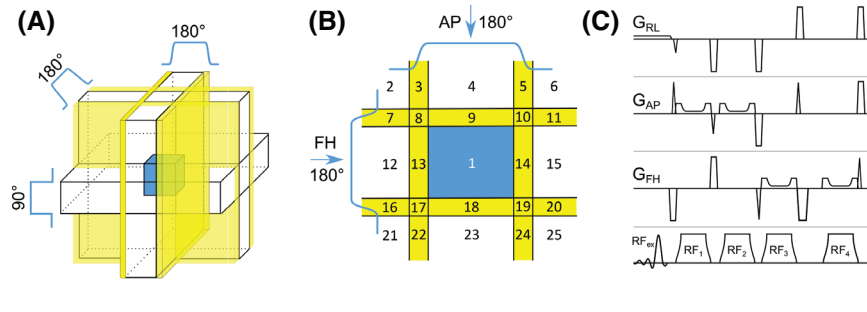


FIGURE 1 A, Schematic of excitation and refocusing slices and volume of interest (VOI; blue box) in an imperfect localization. B, Twenty-five spatial regions are determined by the imperfect refocusing pulses. Yellow bands represent transition areas of the 180° pulses. C, Sequence diagram of the semi-LASER sequence with optimized crusher scheme, assuming that the relatively long slice-selective gradients act as crushers as well. AP, anterior-posterior; FH, feet-head; RL, right-left

3 | METHODS

We adapted the dephasing optimization through coherence order pathway selection (DOTCOPS) algorithm^{14,15} to optimize the relative area of the crushers in the semi-LASER sequence (Table 1) under the assumption that the effective refocusing takes place in the middle of the RF pulse. Therefore, the relatively long slice-selective gradients also act as crushers. Consequently, the area for the crusher between two consecutive adiabatic pulses was calculated as the gradient-time integral of both the slice-selective and the crusher gradients between these two pulses. The area of each individual crusher depended on the orientation along which the pulses were applied, as well as on the polarity of the slice-selective gradients. We applied the excitation along the RL axis and the first and second pairs of refocusing pulses along the AP and FH axes, respectively. The sequence with the optimized crusher scheme is shown in Figure 1C.

3.1 | Data acquisition

We performed the measurements on a 7T MR scanner (Achieva; Philips, Best, Netherlands) using a 32-channel receive-only, eight-channel transmit coil (Nova Medical). To investigate the effects of a large induced magnetic field gradient, the following experiments were carried out on a phantom with a small air bubble. A spectrum was acquired from a voxel of $2 \times 2 \times 2 \text{ cm}^3$ using a semi-LASER sequence with frequency offset-corrected inversion-refocusing pulses.¹⁶ The scan parameters were TE = 31 ms, TR = 5 s, spectral width (SW) = 4 kHz, number of complex points = 2048, number of signal averages (NSA) = 32, a 16-step Cogwheel phase-cycling scheme computed by DOTCOPS,¹⁵ maximum crusher area of $11 \text{ mT m}^{-1} \text{ ms}$, offset frequency = 2.7 ppm, and variable pulse powers and optimized relaxation delays (VAPOR) water suppression.¹⁷ B_0 homogeneity was optimized for the selected volumes by fast, automatic shimming technique by mapping along projections (FASTMAP)¹⁸ with up to second-order shim

terms, second-order projection-based shimming (which is called pencil-beam [PB-2nd] for Philips), using the MRS voxel as a target volume. A B_0 map with the same shim setting as the SV-MRS acquisition was acquired with a 3D fast-field-echo sequence (FOV = $110 \times 110 \times 11 \text{ mm}^3$, matrix size = $64 \times 64 \times 64 \text{ mm}^3$, isotropic resolution = 1.7 mm, flip angle = 8°, delta TE = 1 ms). To determine the spatial origin of spurious signals, CSI data, with only excitation of the MRS single voxel, was acquired. Hence, artifacts will be phase-encoded to their actual sources. The acquisition parameters were FOV = $135 \times 135 \times 120 \text{ mm}^3$, spatial resolution = $15 \times 15 \times 15 \text{ mm}^3$, matrix size = $9 \times 9 \times 8$, excitation volume = $15 \times 15 \times 15 \text{ mm}^3$, NSA = 1, no phase cycling, TE = 31 ms, TR = 5 s, SW = 4 kHz, number of complex points = 2048, offset frequency = 2.7 ppm, and scan time = 54:25 min. The same SV and CSI experiments with the same acquisition parameters as the experiments described previously were performed on a phantom without an air bubble.

The in vivo study was approved by the local ethical committee, and written informed consent was obtained from the participants. We included 2 subjects (male/female, age: 31/32 years) who underwent similar MR protocols. A T_1 -weighted anatomical image (T_1 3D turbo field echo: 1.5 mm^3 isotropic voxel) was acquired to position the MRS voxels in the frontal cortex. The same semi-LASER single voxel measurement as in the phantom was performed on a volume of $2 \times 2 \times 2 \text{ cm}^3$. Another spectrum was acquired with the same protocol but with reversed gradient polarity along the FH direction. Like the phantom experiments, a B_0 map (PB-2nd) was acquired with a 3D fast field echo with a FOV = $224 \times 224 \times 140 \text{ mm}^3$, matrix size = $64 \times 64 \times 40 \text{ mm}^3$, and isotropic resolution of 3.5 mm. In the second volunteer, we first acquired the CSI data with the following parameters: FOV = $210 \times 210 \text{ mm}^2$, slice thickness = 30 mm, spatial resolution = $30 \times 30 \times 30 \text{ mm}^3$, matrix size = $7 \times 7 \times 6$, excitation volume = $30 \times 30 \times 30 \text{ mm}^3$, NSA = 1, TE = 31 ms, TR = 5 s, SW = 4 kHz, number of complex points = 2048, offset frequency = 2.7 ppm, and scan time = 19 min).

TABLE 1 Relative crusher areas and optimized phase-cycling scheme (a 16-step Cogwheel phase cycling) obtained from the DOTCOPS tool

| Semi-LASER sequence | RF pulse number | Relative crusher area along RL | Relative crusher area along AP | Relative crusher area along FH |
|-------------------------------------|-----------------|--------------------------------|--------------------------------|--------------------------------|
| DOTCOPS (COG16 [0, 9, 7, 9, 0; 10]) | 1 | 0 | 1 | -1 |
| | 2 | -1 | 1 | 1 |
| | 3 | -1 | -0.7252 | 0.2743 |
| | 4 | 1 | 0.2743 | -0.7252 |
| | 5 | 1 | 1 | 1 |

Note: The maximum crusher area of $11 \text{ (mT m}^{-1} \text{ ms)}$ was assigned to the crushers with relative area of 1.

Abbreviation: DOTCOPS, dephasing optimization through coherence order pathway selection.

Subsequently, we repeated the SV-MRS acquisition but with voxel size of $3 \times 3 \times 3 \text{ cm}^3$, NSA = 16, and no phase cycling (similar to the 3D CSI). The B_0 shim settings were not adjusted as to maintain the same B_0 field as during the acquisition of the 3D-CSI and the SV-MRS experiment. We also acquired whole-brain B_0 maps for further comparisons.

3.2 | Finding the source of spurious signals

The magnitude images acquired from the 3D fast field echo sequence were used for masking out the background noise in the B_0 map. Residual noise from neck and nose were removed with morphological filters, a combination of closing and opening morphological operations with a disk-shaped structuring element tuned empirically (the radius of 1 and 7 pixels, respectively) (Supporting Information Figure S1). We used PulseWizard (a *MATLAB*-based RF pulse generation and simulation graphical user interface available for downloading from Robin A. de Graaf's Yale University profile webpage) to determine the width of the transition bands of the refocusing pulses in the B_0 map. Approximately, one voxel of the in vivo (isotropic resolution = 3.5 mm) B_0 map and two voxels of the phantom (isotropic resolution = 1.7 mm) B_0 map covered the transition bands of the refocusing pulses for a 2-cm isotropic MRS voxel.

For each coherence pathway, voxels in the B_0 map were investigated for the possibility of signal phase cancellation by the crushers in the acquisition window (t_{reph}) of 100 ms (with lower and upper threshold of TE and TE + 100 ms) along three spatial axes, as mentioned in section 2. To visualize the effect of all coherence pathways, we created the source of spurious signals map (SoSS map) of all pathways.

This map shows the number of pathways for each voxel in the B_0 map, where $\phi_{crusher,i}$ satisfied the inequality condition described in Eq. 4.

3.3 | Quantifying number of voxels as potential sources of spurious signals

We assessed the effect of reversing the polarity of the gradients in one direction in the appearance of spurious signals, both experimentally and by simulation. To find the relation between the total crusher areas and the number of voxels emerging as potential sources of spurious signals, we simulated an increased total crusher area along each spatial dimension with a factor starting from 1 up to 20 by 25% increments (ie, crushing factors). We also performed the same simulation while reversing the polarity of the gradients along one of the spatial directions (FH axis).

4 | RESULTS

4.1 | Phantom data

The location of the MRS voxel in the phantom with the air bubble and the corresponding spectrum acquired by the semi-LASER sequence (without phase cycling) is shown in Figure 2A. A clear local B_0 gradient at the air-solution interface can be seen in the B_0 map (Figure 2B). In the spectrum, spurious signals can be observed in the frequency range of 4.0–4.6 ppm. Figure 2B depicts the SoSS map overlaid on the two corresponding slices of the B_0 map (second-order VOI shim) and color-coded according to the number of coherence pathways that lead to spurious signals. These slices are within the CSI grid (Figure 2C) and visualize locations where the signal dephasing caused by crusher gradients and B_0 field gradients canceled out. Analysis of the coherence pathways showed that the spurious signals mostly arise from locations around the air bubble area. This is confirmed by the CSI data, showing the spatial origin of the spurious signals around the air bubble (Figure 2C). In addition, spurious signals also arise from voxels at the edge of the phantom, which can be verified by the data in the bottom rows in the CSI grid. Figure 3 shows

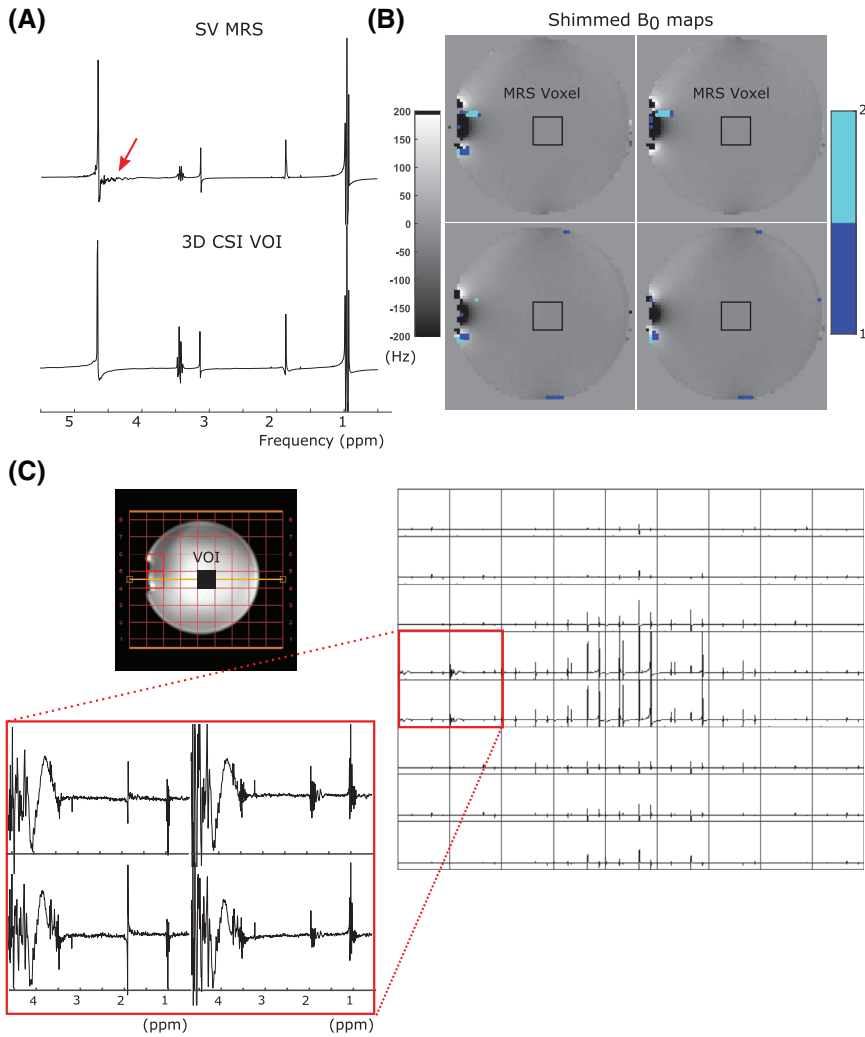


FIGURE 2 A, Spectra from a phantom containing a small air bubble, using single-voxel (SV) semi-LASER (no phase cycling) and CSI with the same VOI localization as the single voxel. Compared with the VOI of the CSI, SV MRS exhibits some spurious signals indicated by red arrow. B, The MRS voxel localized on the shimmed B₀ map (PB-2nd VOI shim). The possible origins of spurious signals were overlaid on representative slices of the B₀ map and color-coded according to the number of pathways associated with these regions. These slices are within the CSI grid (shown in [C]) and visualize locations where the signal dephasing due to crusher gradients and B₀ field gradients canceled out, for those pathways. C, The CSI data confirmed the same locations of artifact (air bubble and the edge of the phantom) as the B₀ map analysis. The spectra were scaled to the SD of the noise

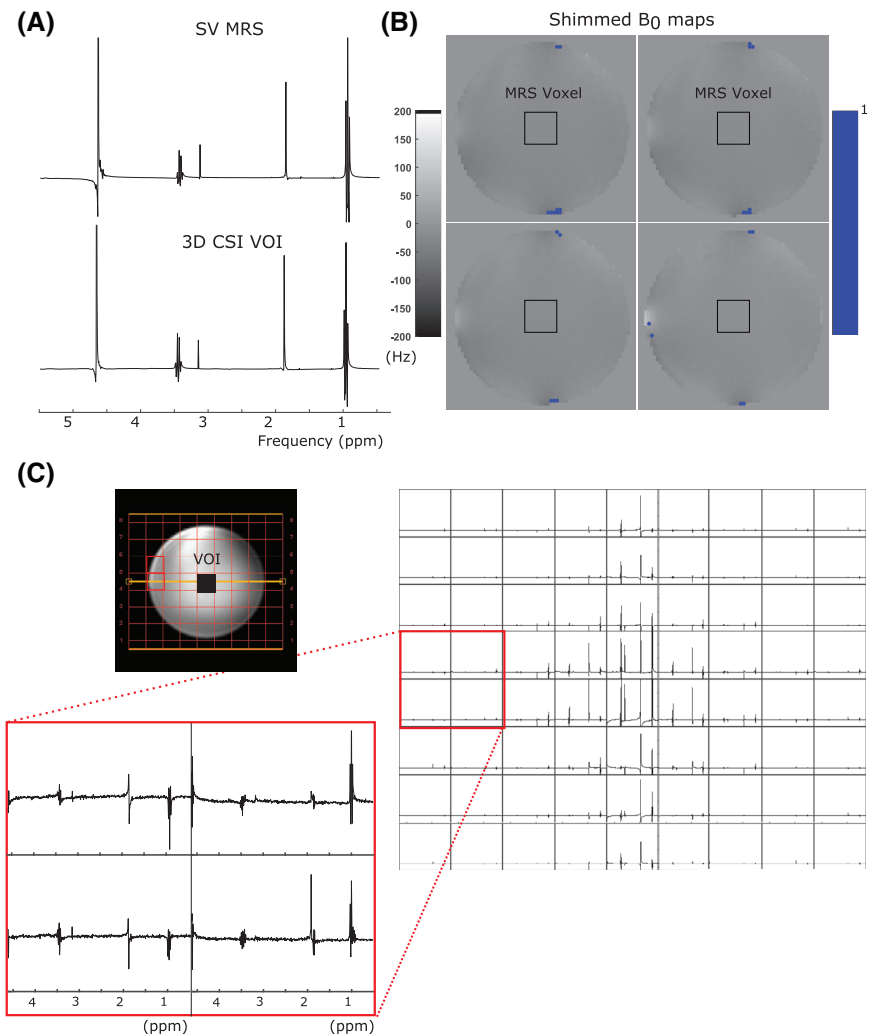
the results of the same phantom when fully filled with water. Compared with the spectra in Figure 2, no spurious signals can be seen in the CSI grid, which is confirmed by the SoSS map (Figure 3B).

4.2 | In vivo data

Among all 80 unwanted coherence pathways, we identified $[00-1-1-1]$ as the coherence pathway with the least total crushing area ($\|\phi_{\text{crusher},i}\|$), which will serve here as an example. This pathway originated from areas 8-10-17-19 and 3-5-22-24 in Figure 1B. These areas corresponded to voxels that were confined to the transition areas of the refocusing pulses in the AP, inside and outside of the FH bands, respectively. The spurious signals from the $[00-1-1-1]$ coherence pathway was most likely to get rewound by the inhomogeneity gradients in the acquisition window. As an example, Figure 4A shows sagittal slices of the B₀ map, in which the red voxels depict the locations where the signal dephasing due to

the inhomogeneity gradient ($\phi_{\text{inhom.gr},i}$) and crusher gradients ($\phi_{\text{crusher},i}$) of the $[00-1-1-1]$ pathway from regions 3-5-22-24 were canceled at a specific time between TE and TE + 100 ms. The voxels causing potential spurious signals are most densely packed in the vicinity of the skull or near the air cavity with large magnetic-field inhomogeneities. Figure 4B shows the result of the same analysis, but inverting the gradient polarity along one of the spatial dimensions (FH axis). When reversing the gradient polarity, fewer locations where spurious signals could arise from were identified in the selected slices. The SoSS maps are shown in Figure 5, where it can be seen that for this MRS voxel, which was placed in the frontal lobe, most potential sources of spurious signals were located close to the skull and around the air cavities. By reversing the gradient polarity, voxels that were detected as a source of spurious signals in more than five pathways disappeared. New spurious signal locations, however, appeared throughout the brain (see Supporting Information Figure S2 for more example slices). In contrast to the local MRS VOI shim, a cluster of voxels was detected in the transition bands adjacent to

FIGURE 3 Resulting spectra and source of spurious signals (SoSS) maps of the phantom without air bubble from the same SV and CSI experiments as in Figure 2. The CSI and SoSS maps show no such artifacts as observed in the phantom with an air bubble. The spectra were scaled to the SD of the noise



the MRS voxel in the case of whole-brain shim (Supporting Information Figure S3). Moreover, voxels associated with more than three different pathways were located in the transition area number 19 (Supporting Information Figure S3A,B; white arrows).

Reversing the gradient polarity along one axis resulted in fewer spurious signals in the frequency range of 3.3–4.2 ppm (Figure 6A). The spectra from SV MRS (average of 16 NSAs, no phase cycling) and from the VOI of the 3D-CSI data (1 NSA) are shown in Figure 6B. Although the spectral quality of the SV MRS acquired without phase cycling seemed reasonable, there appeared to be spurious signals compared with the CSI data with the same VOI as the SV MRS. Moreover, substantial spurious signals in the CSI grid outside the presumably selected MRS voxel are observable.

The effect of an increasing crusher area on the number of voxels being identified as potential sources of spurious signals was simulated and shown in Figure 7. An increase in the total crusher area resulted in fewer potential locations of spurious signals. However, even when multiplying

the total crushing area by a factor of 10, still several potential locations led to spurious signals. For instance, with a 10-fold increase in the crushing factor (section 3), the number of voxels that could be the source of spurious signals was decreased by 91.3% and 97.7% in the case of VOI and whole-brain shims, respectively. The number of voxels that could lead to spurious signals in the case of inverted gradients polarity was not less than the noninverted ones for all crushing factors. The total number of spurious signal locations decreased faster with whole-brain shim.

5 | DISCUSSION

We presented a method to identify the locations where spurious signals in SV MRS could originate from investigation of all possible coherence pathways in a semi-LASER sequence. We identified possible spurious signal sources in the B₀ map by localizing voxels in which the phase evolution induced by the crusher gradients was reversed by the local magnetic-field inhomogeneities. The a priori

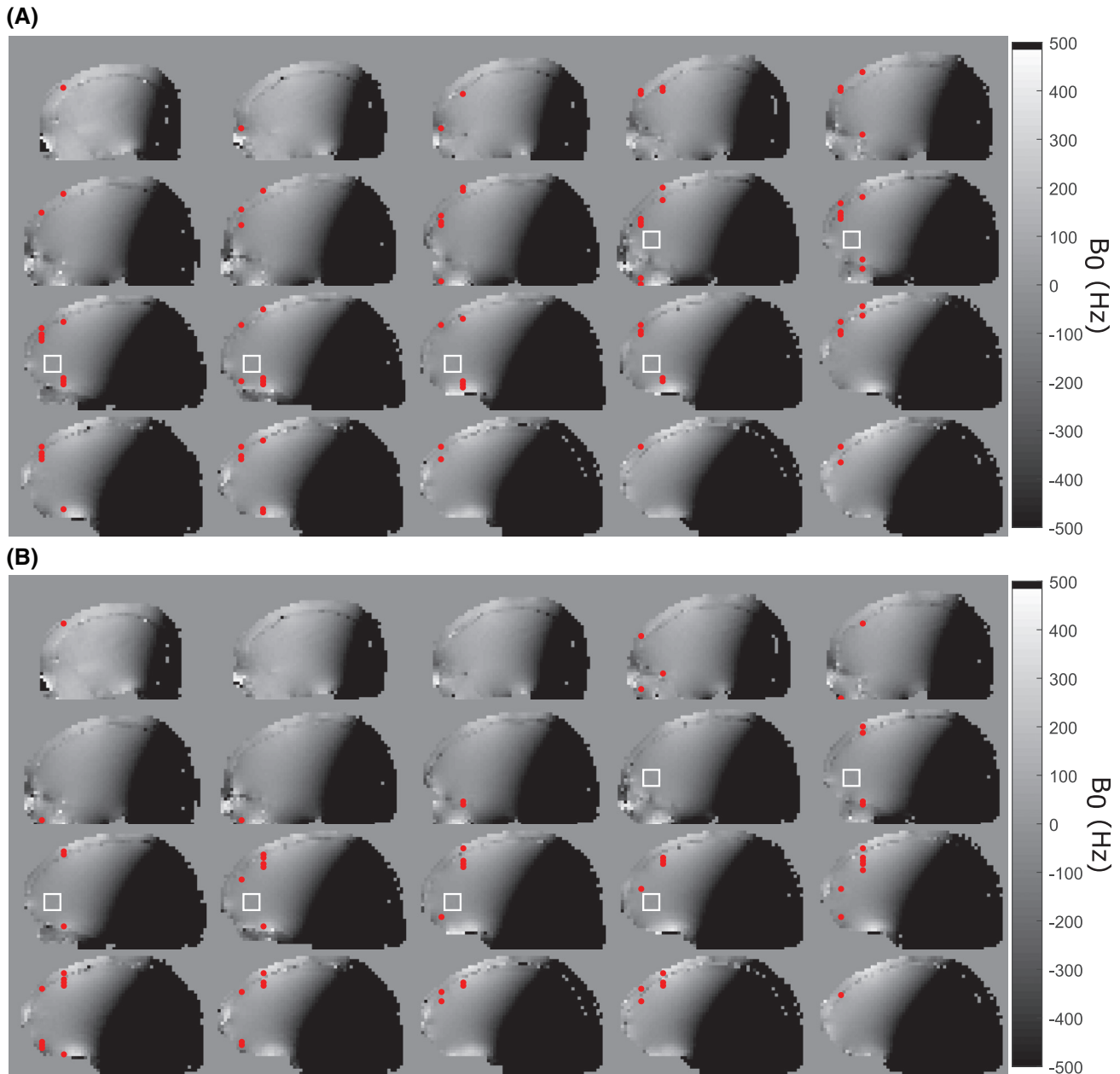


FIGURE 4 Representative sagittal slices of the B_0 map (PB-2nd VOI shim) inside and outside of the MRS voxel (white square). The voxels in red show the locations where the magnetic-field inhomogeneity gradient potentially causes a spurious signal (Eq. 4) by canceling out the effect of external gradients through pathway $[00 -1 -1 -1]$ for the crusher scheme in Figure 1C (A) and when the gradient polarity was inverted along the FH axis (B)

identification of the source of spurious signals can help to optimize pulse sequences. Our results show that the potential spurious signals do not arise from a single location but are scattered throughout the head. At ultrahigh field (ie, 7 T), the B_0 field is less uniform than at lower field strength. This increases the chance that the signal dephasing due to the local B_0 field inhomogeneity and crusher gradients cancel each other. However, this nonuniformity scales linearly with magnetic field strength, thereby affecting SV MRS at lower fields as well, but to a lesser extent.

Possible solutions to reduce spurious signals include improved crusher schemes, phase cycling, outer-volume suppression, CSI, and sensitivity encoding.¹⁸ Phase cycling is a method to suppress the spurious signals by subtracting the signals from undesired coherence pathways. However, its efficacy will decrease in the presence of phase and frequency instability and motion. Outer-volume suppression adds additional saturation pulses to minimize longitudinal magnetization before the excitation pulse. Our proposed methodology can guide placement of

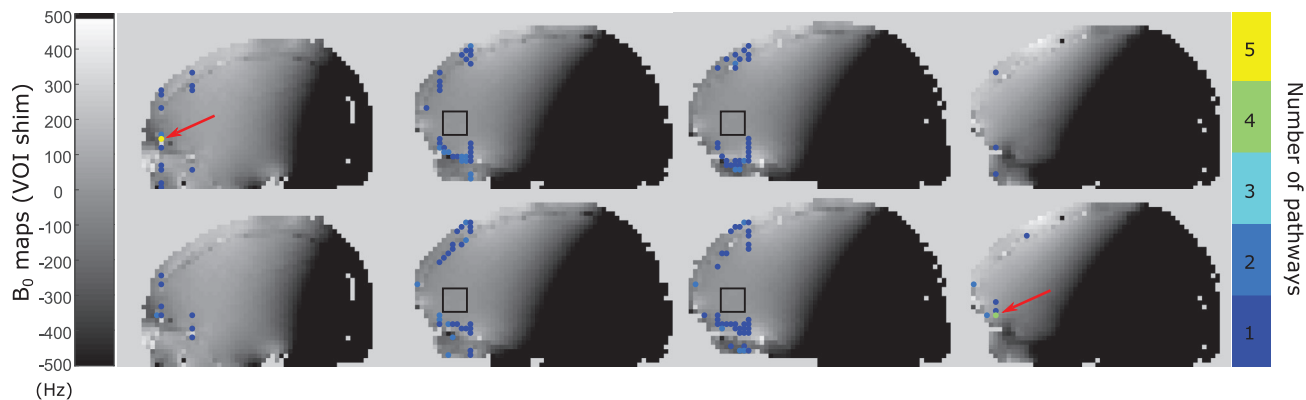


FIGURE 5 The SoSS maps of all possible pathways overlaid on the B_0 map (PB-2nd VOI shim) for the optimized crusher scheme in Figure 1C (top row) and (the same scheme with inverted polarity of the gradients along FH direction bottom row). The SoSS maps show the spurious signal origins and the number of pathways (color-coded) associated with them. At these voxels, $\phi_{\text{crusher},i}$ satisfied Eq. 4 ($\|\phi_{\text{inhom.gr},i}(x, y, z; \text{TE})\| \leq \|\phi_{\text{crusher},i}\| \leq \|\phi_{\text{inhom.gr},i}(x, y, z; \text{TE} + 100 \text{ ms})\|$). The red arrows indicate the locations where the associated number of pathways that could lead to potential spurious signals is greater than three (see Supporting Information Figure S2 for more example slices). The MRS voxel is shown as a black box

slice-selective outer-volume suppression pulses, although additional pulses in the pulse sequence might lead to increased chances of spurious signals. The phase encoding in CSI moves the spurious signals to the location of its origin. However, it requires a long acquisition time; therefore, typically no signal averaging is performed, and hence no phase cycling can be done. Faster MRSI methods¹⁹ can shorten the scan time, but this has rarely been implemented. With sensitivity encoding, the coil sensitivity maps from a multichannel receive coil can be used for spatial separation of the spurious signals and the desired spectrum. Our method can be used as an input to such an algorithm, although the many scattered spurious signal locations, as demonstrated here, could render efficient unfolding impossible.

The voxels that were identified through multiple coherence pathways were located in the areas 8, 10, 17, and 19. Most of the coherence pathways also originated from these areas. Investigating an individual coherence pathway may give valuable insight into further sequence development. This may require alternative strategies, like the use of local crusher gradients,²⁰ dynamic multicoil shimming,²¹ or elliptical localization with pulsed second-order field.²² Accurately identifying the location of the artifacts will also enable simulating the spectral appearance of spurious signals. This paves the way to use artificial intelligence to remove spurious signals from the data.²³

We identified the possible source of spurious signals based on the combination of the sequence crusher scheme and the B_0 map. The SoSS maps were generated to quantify the influence of all coherence pathways associated with possible spurious signal locations. Polarity reversal of all gradients can reduce the appearance of spurious signals

and improve localization by incorporating the spatial B_0 information. Even though we saw fewer spurious signals in the spectrum after inverting the gradient polarity, the number of potential sources of spurious signals in the B_0 map did not decrease. This could be due to the fact that, here, we only looked into the number of potential sources of spurious signals, and not into their intensities.

Increasing the crusher area can also help reduce the possible sources of spurious signals and this relation can be optimized upfront for improved crushing of signals from unwanted coherence pathways. This is, however, at the cost of increased TE and stronger gradients, which will increase the chances of peripheral nerve stimulation. Moreover, the increase in the crusher area by itself is not sufficient for removing all sources of spurious signals. In simulation, we showed that even with very high crushing factors (section 3), the number of potential spurious signal locations reaches a nonzero plateau (Figure 7). It should be noted that, practically, for this sequence implementation, the total crusher area can only be increased with a maximum of 75% while maintaining a TE of 31 ms.

Comparing the two brain shims, the density of the possible source of spurious signals was more notable at the edge of the MRS voxel in the situation of the whole-brain shim than in the local VOI shim (Supporting Information Figure S3 and Figure 5). The local VOI shim (PB-2nd) resulted in lower SD of the field homogeneity in the MRS voxel compared with the whole-brain shim (5.0 Hz vs 20.1 Hz). The total number of spurious signal locations for the whole-brain shim was higher compared with the local VOI shim for the first crushing factors (Figure 7), but it decreased faster with increasing crushing factor. The polarity reversal did not reduce the abundance of potential

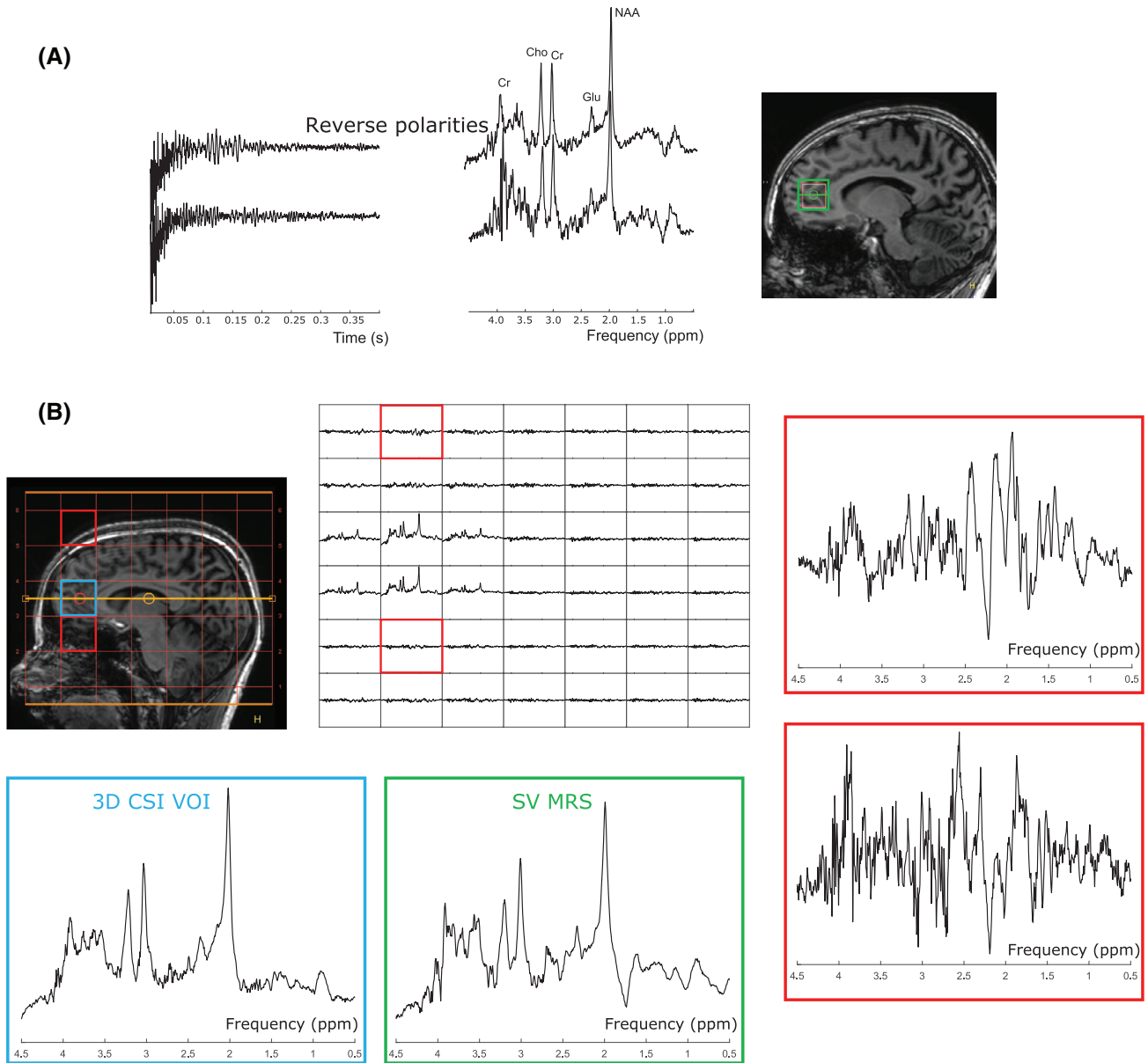


FIGURE 6 Spectrum acquired with the semi-LASER scheme in Figure 1C with PB-2nd VOI shim setting. A, Time and frequency-domain signals from a voxel of $2 \times 2 \times 2 \text{ cm}^3$. The resulting FID and spectrum after gradients polarity reversal are shown on top. B, Spectra from 3D CSI (blue box; number of signal averages [NSA] = 1, matrix size = 7 [AP] \times 7 [RL] \times 6 [FH]) with the same localization as SV MRS (green box; semi-LASER, TE = 31 ms). Compared with SV MRS, the VOI spectrum exhibits less amount of artifacts. The red boxes depict the locations in CSI data from where possible spurious signals originate (Figure 4). Cho, choline; Cr, creatine; Glu, glutamate; NAA, N-acetylaspartate

spurious signal locations in the very first crushing factors; however, it is worth mentioning that the location of voxels, identified as sources of spurious signals, appears to be the driving force behind the appearance of spectral artifacts and not the number of voxels. Moreover, a good B_0 shimming (typically linewidth $< 15 \text{ Hz}$) in SV MRS is essential to decrease the linewidth within the voxel and to have an efficient water suppression.²⁴ For that, higher-order shimming within the voxel can be used, although it could result in large frequency offsets outside the voxel. This

consequently affects the global water suppression and increases the chance of spurious signals being generated outside the MRS voxel. Therefore, enhanced overall water suppression as a result of improved global shimming can help reduce spurious signals.²⁵

Our method to determine the spatial origin of spurious signals in SV MRS was validated both in phantom and in vivo experiments. In the 3D-CSI acquisition, the phase-encoding gradients were applied in three directions. Therefore, spurious signals experienced phase-encoding

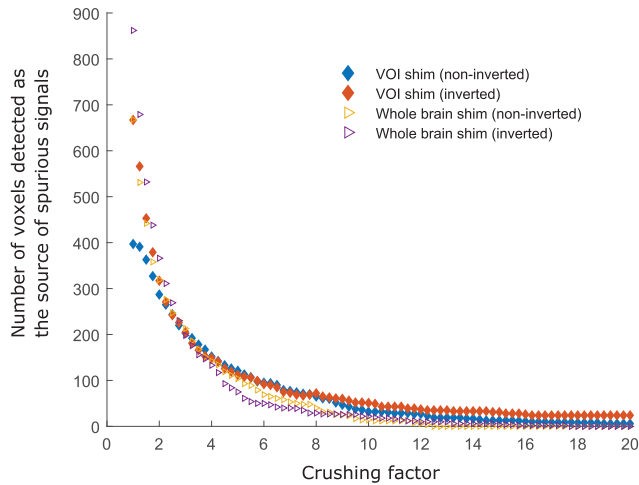


FIGURE 7 The effect of increasing the crushing area (scheme in Figure 1C) on the number of voxels being detected as potential sources of spurious signals based on PB-2nd VOI shim and second-order whole-brain shim. The x -axis values represent the factor by which the crushing area was increased. Crushing factors of 1 and 1.25 (first and second point in the graph) indicate the current total crusher area and current total crusher area \times 1.25, respectively. For the crusher scheme in Figure 1C with TE = 31 ms, only the first four crushing factors would be practical

gradients in three directions and did not fold into the MRS voxel. We observed that the spurious signals originated from the same locations as the locations identified by our B_0 map analysis. In vivo, the non-phase-cycled SV MRS showed significant spurious signals, even with an optimized crusher scheme. The in vivo CSI data confirmed that spurious signals in SV MRS originated from outside the voxel of interest, even when taking the point spread function into account.

We used a simplified model for the determination of all possible coherence pathways; therefore, our methods have some limitations. First, for analysis of the coherence pathways, we assumed that the 90° excitation pulse had a perfect rectangular excitation profile. We also assumed that the transition bands of the 180° refocusing pulses experienced 90° excitation, while the spins in these areas could experience a flip angle from 0° to 180° , depending on spatial location. These assumptions primarily affect the intensity of the spurious signal, but they do not affect the chance of the crusher area being counterbalanced by the local B_0 inhomogeneity gradients. Second, in our analyses, we considered a time window of 100 ms to investigate the possibility of signal rephasing by the local inhomogeneity gradient, because after 100 ms, most of the signal has been decayed due to T_2^* (considering the T_2^* values in the brain). Looking at the time-domain signals in Figure 6A, the FID before inverting the gradient polarity exhibited a greater amount of spurious echoes (> 0.18 s).

This observation might explain the appearance of spurious signals up-field of water in the frequency domain. Finally, our presented method lacks the ability to identify which unwanted coherence pathways are most destructive to the spectrum. It would be of interest to determine those pathways that manifest spurious signals in the spectrum more than the others. This would enable the design of crusher optimization algorithms to provide targeted crushing power toward those specific pathways.

6 | CONCLUSIONS

This analysis allows us to relate spurious signals to their specific anatomical locations of origin and therefore opens a new window to optimize the acquisition strategy. Knowing the possible sources of spurious signals, one can opt for changing the gradients polarity, shimming differently, or increasing crusher strength at the cost of prolonged TE. This prior knowledge will help design a crusher scheme that effectively sorts out spurious signals from experimental data. Our method can facilitate MRS-sequence design to be more robust to spurious signals.

ACKNOWLEDGMENT


The authors thank Alex Bhogal for helping with proof-reading, and Hanna Liu for discussion on mathematical formulations.

ORCID

Zahra Shams  <https://orcid.org/0000-0002-0311-0665>

Dennis W. J. Klomp  <https://orcid.org/0000-0002-5884-5386>

Vincent O. Boer  <https://orcid.org/0000-0001-6026-3134>

Jannie P. Wijnen  <https://orcid.org/0000-0003-2352-3667>

Evita C. Wieggers  <https://orcid.org/0000-0001-5451-2990>

REFERENCES

- de Graaf RA. *In Vivo NMR Spectroscopy*. John Wiley & Sons; 2019.
- Öz G, Alger JR, Barker PB, et al. Clinical proton MR spectroscopy in central nervous system disorders. *Radiology*. 2014;270:658-679.
- Bolan PJ, Kim E, Herman BA, et al. MR spectroscopy of breast cancer for assessing early treatment response: results from the ACRIN 6657 MRS trial. *J Magn Reson Imaging*. 2017;46:290-302.
- Bhogal AA, Schür RR, Houtepen LC, et al. 1H-MRS processing parameters affect metabolite quantification: the urgent need for uniform and transparent standardization. *NMR Biomed*. 2017;30:e3804.
- Kreis R. Issues of spectral quality in clinical 1H-magnetic resonance spectroscopy and a gallery of artifacts. *NMR Biomed*. 2004;17:361-381.

6. Scheenen TWJ, Klomp DWJ, Wijnen JP, Heerschap A. Short echo time 1H-MRSI of the human brain at 3T with minimal chemical shift displacement errors using adiabatic refocusing pulses. *Magn Reson Med.* 2008;59:1-6.
7. Boer VO, van Lier ALHMW, Hoogduin JM, Wijnen JP, Luijten PR, DWJ K. 7-T 1H MRS with adiabatic refocusing at short TE using radiofrequency focusing with a dual-channel volume transmit coil. *NMR Biomed.* 2011;24:1038-1046.
8. Wilson M, Andronesi O, Barker PB, et al. Methodological consensus on clinical proton MRS of the brain: review and recommendations. *Magn Reson Med.* 2019;82:527-550.
9. Bain AD. Coherence levels and coherence pathways in NMR. A simple way to design phase cycling procedures. *J Magn Reson.* 1984;56:418-427.
10. Keeler J. Understanding NMR spectroscopy. *Choice Rev Online.* 2006;43:5896.
11. Ernst T, Chang L. Elimination of artifacts in short echo time 1H MR spectroscopy of the frontal lobe. *Magn Reson Med.* 1996;36:462-468.
12. Moonen CTW, Sobering G, Van Zijl PCM, Gillen J, Von Kienlin M, Bizzi A. Proton spectroscopic imaging of human brain. *J Magn Reson.* 1992;98:556-575.
13. Starck G, Carlsson Å, Ljungberg M, Forssell-Aronsson E. k-Space analysis of point-resolved spectroscopy (PRESS) with regard to spurious echoes in in vivo ¹H MRS. *NMR Biomed.* 2009;22:137-147.
14. Landheer K, Juchem C. Dephasing optimization through coherence order pathway selection (DOTCOPS) for improved crusher schemes in MR spectroscopy. *Magn Reson Med.* 2019;81:2209-2222.
15. Landheer K, Juchem C. Simultaneous optimization of crusher and phase cycling schemes for magnetic resonance spectroscopy: an extension of dephasing optimization through coherence order pathway selection. *Magn Reson Med.* 2020;83:391-402.
16. Arteaga de Castro CS, Boer VO, Andreychenko A, et al. Improved efficiency on editing MRS of lactate and γ -aminobutyric acid by inclusion of frequency offset corrected inversion pulses at high fields. *NMR Biomed.* 2013;26:1213-1219.
17. Tkáč I, Gruetter R. Methodology of 1H NMR spectroscopy of the human brain at very high magnetic fields. *Appl Magn Reson.* 2005;29:139-157.
18. Berrington A, Považan M, Barker PB. Estimation and removal of spurious echo artifacts in single-voxel MRS using sensitivity encoding. *Magn Reson Med.* 2021;86:2339-2352.
19. Bogner W, Otazo R, Henning A. Accelerated MR spectroscopic imaging—a review of current and emerging techniques. *In NMR in Biomedicine.* John Wiley and Sons; 2020.
20. Boer VO, van de Lindt T, Luijten PR, Klomp DWJ. Lipid suppression for brain MRI and MRSI by means of a dedicated crusher coil. *Magn Reson Med.* 2015;73:2062-2068.
21. Juchem C, Nixon TW, McIntyre S, Boer VO, Rothman DL, De Graaf RA. Dynamic multi-coil shimming of the human brain at 7 T. *J Magn Reson.* 2011;212:280-288.
22. de Graaf RA, Brown PB, De Feyter HM, McIntyre S, Nixon TW. Elliptical localization with pulsed second-order fields (ECLIPSE) for robust lipid suppression in proton MRSI. *NMR Biomed.* 2018;31:e3949.
23. Kyathanahally SP, Döring A, Kreis R. Deep learning approaches for detection and removal of ghosting artifacts in MR spectroscopy. *Magn Reson Med.* 2018;80:851-863.
24. Juchem C, Cudalbu C, Graaf RA, et al. B₀ shimming for in vivo magnetic resonance spectroscopy: experts' consensus recommendations. *NMR Biomed.* 2021;34:e4350.
25. Boer VO, Andersen M, Lind A, Lee NG, Marsman A, Petersen ET. MR spectroscopy using static higher order shimming with dynamic linear terms (HOS-DLT) for improved water suppression, interleaved MRS-fMRI, and navigator-based motion correction at 7T. *Magn Reson Med.* 2020;84:1101-1112.

SUPPORTING INFORMATION

Additional supporting information may be found in the online version of the article at the publisher's website.

Figure S1. A, Magnitude images acquired from the 3D fast-field-echo (FFE) sequence. B, Sagittal slices of the pencil-beam volume second-order volume-of-interest (VOI) shim maps after intensity-based thresholding to remove noise in the background and at the air-tissue interfaces. C, Final B₀ maps after applying morphological filters. B₀ map color bars are in hertz units

Figure S2. Source of spurious signals (SoSS) maps overlaid on representative sagittal slices of the B₀ map (second-order VOI shim) for the scheme in Figure 1 with inverted gradients polarity along the feet-head (FH) axis. These maps show the potential locations of the spurious signals and the number of pathways (color-coded) associated with them. At these voxels, $\varphi_{\text{crusher},i}$ satisfied Eq. 4: ($\|\varphi_{\text{inhom.gr},i}(x,y,z; TE)\| \leq \|\varphi_{\text{crusher},i}\| \leq \|\varphi_{\text{inhom.gr},i}(x,y,z; TE + 100 \text{ ms})\|$)

Figure S3. The SoSS maps for representative sagittal slices of the whole-brain shim maps for the scheme in Figure 1 (A) and the same scheme with inverted gradients polarity along FH axis (B). The SoSS maps show the spurious signals origins and the number of pathways (color-coded) associated with them. At these voxels, $\varphi_{\text{crusher},i}$ satisfied Eq. (4) ($\|\varphi_{\text{inhom.gr},i}(x,y,z; TE)\| \leq \|\varphi_{\text{crusher},i}\| \leq \|\varphi_{\text{inhom.gr},i}(x,y,z; TE + 100 \text{ ms})\|$). White arrows indicate voxels being identified in more than three pathways.

How to cite this article: Shams Z, Klomp DWJ, Boer VO, Wijnen JP, Wiegers EC. Identifying the source of spurious signals caused by B₀ inhomogeneities in single-voxel ¹H MRS. *Magn Reson Med.* 2022;88:71-82. doi: 10.1002/mrm.29222